frontiers | Frontiers in Earth Science

TYPE Original Research
PUBLISHED 05 February 2025
DOI 10.3389/feart.2025.1499268

OPEN ACCESS

EDITED BY
Manoj Khandelwal,
Federation University Australia, Australia

REVIEWED BY
Qibin Lin,
University of South China, China
Jiaqi Guo,
Henan Polytechnic University, China

*CORRESPONDENCE
Xianda Feng,
cea_fengxd@ujn.edu.cn

RECEIVED 20 September 2024
ACCEPTED 08 January 2025
PUBLISHED 05 February 2025

CITATION
Yuan Z, Cao Y, Zhang T, Li S and Feng X (2025) Effects of inclination angle and unloading rate of confining pressure on triaxial unloading-induced slip behaviors of shale fractures.
Front. Earth Sci. 13:1499268.
doi: 10.3389/feart.2025.1499268

Effects of inclination angle and unloading rate of confining pressure on triaxial unloading-induced slip behaviors of shale fractures

Zhe Yuan[1,2], Yongna Cao[2], Tao Zhang[2,3], Shuchen Li[4] and Xianda Feng[5]*

[1]Highway School, Chang'an University, Xi'an, China, [2]Jinan Traffic Engineering Quality and Safety Center, Jinan, China, [3]School of Mechanics and Civil Engineering, China University of Mining and Technology, Xuzhou, China, [4]School of Future Technology, Shandong University, Jinan, China, [5]School of Civil Engineering and Architecture, University of Jinan, Jinan, China

The effects of inclination angle θ and unloading rate of confining pressure U_c on the unloading-induced slip behaviors of shale fractures were investigated by conducting triaxial unloading-induced fracture slip experiments. The variations in mechanical stability, frictional behavior, and morphology variation of shale fractures were systematically explored. The results show that with the continuous unloading of confining pressure, the fractures were initiated to slip, then entered the quasi-static slip stage, and eventually entered the dynamic slip stage in sequence. The occurrence of stick-slip events in the quasi-static slip stage was strongly influenced by the θ and U_c. As θ increases from 30° to 50°, the stick-slip events occurred from 0 to 3 times and from 1 to 3 times for U_c = 0.1 MPa/min and 1 MPa/min, respectively. The θ and U_c have a great influence on the interaction mode of the fractures, which directly affects the frictional behavior of the fractures. The slipping failure behavior of the fracture surfaces is mainly controlled by θ, while U_c plays different roles for the samples with different θ. With the increase in θ, the interaction form between asperities during the slip process may be changed into non-tight contact stage. The increase in θ may enhance or weanken the anisotropy of JRC, depending on whether the U_c reached a certain rate between 0.1 MPa/min and 1 MPa/min. Our results may shed light on the seismicity mitigation and safe exploitation of shale gas.

KEYWORDS

inclination angle, unloading rate of confining pressure, triaxial unloading-induced slip, slip behavior, shale fracture

1 Introduction

In recent years, to reduce carbon emissions and ensure energy security, the primary composition of the energy structure is transitioning from traditional energy to renewable

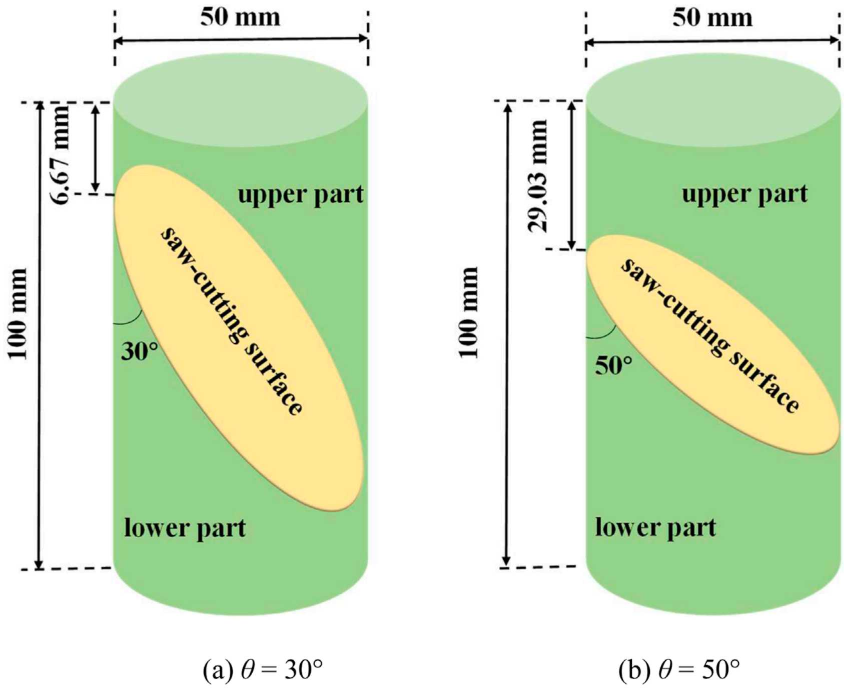

FIGURE 1
Geometrical information of the saw-cut shale fractures with different inclination angles θ: **(A)** θ = 30°, **(B)** θ = 50°.

energy worldwide (Hou et al., 2021; Sun et al., 2021; Zhang et al., 2022; Zhu et al., 2023; Yang et al., 2024; Ye et al., 2024). The shale gas is renewable, clean and highly efficient, and related industry is blooming in many countries (Cao et al., 2018; Hu et al., 2021; Lei et al., 2023; Tan et al., 2023; Wang et al., 2023). In order to realize the productive development of shale gas, the matrix of shale gas reservoir with ultra-low porosity and low permeability is typically hydro-fractured to make substantial fractures, which allows the outflow of shale gas emitting from the reservoir (Loucks et al., 2009; Wang et al., 2016). During the process of hydro-fracturing, abundant fluid is continuously injected into the reservoirs to artificially create the fractures (Liu et al., 2024). The pore pressure increases a lot and the effective normal stress acting on the natural fractures or faults significantly decreased due to the injection of fluid, which brings the fractures closer to the unstable state (Passelègue et al., 2018; Wang et al., 2020; Moein et al., 2023; Zhu et al., 2024). And the natural fractures may be activated to slip in this way, even triggering many seismic events (Bourne et al., 2018; Langenbruch and Zoback, 2016; Kivi et al., 2022). For instance, the moment magnitude (M_w) 4.6 earthquake occurred in British Columbia in 2015, the M_w 5.7 earthquake occurred in Sichuan in 2019, the surface wave magnitude (M_s) 6.0 earthquake occurred in Luxian in 2021 (Lei et al., 2017; Zhao et al., 2023; Meng et al., 2019; Wang et al., 2021). These three devastating seismic events were presumed to be related to hydro-fracturing process (Lei et al., 2019; Moein et al., 2023). Hence, it is an imperative to reveal the mechanism of fracture activation linked with the hydro-fracturing for the safe exploitation of shale gas.

Several studies have conducted to explore the activation mechanism and slip behavior of fractures (He et al., 2014; Wu et al., 2014; Ye and Ghassemi (2018); Eshiet and Sheng, 2017; Feng et al., 2021; Ji et al., 2019; Zhou et al., 2023). Wu et al. (2014) experimentally investigated the effect of unloading of normal stress on the frictional slip process of fractures under constant shear stress conditions. They found that the stress drop and the generated shear displacement during the slipping process were strongly correlated with the initial stress state of fractures. Ji et al. (2019) conducted unloading-induced slip experiments on the sawcut and tensile fractures, and the influence of unloading rate of normal

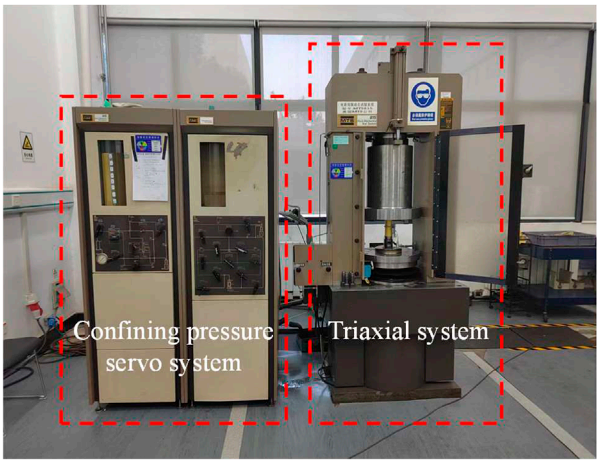

FIGURE 2
The MTS 815.02 rock mechanics testing system.

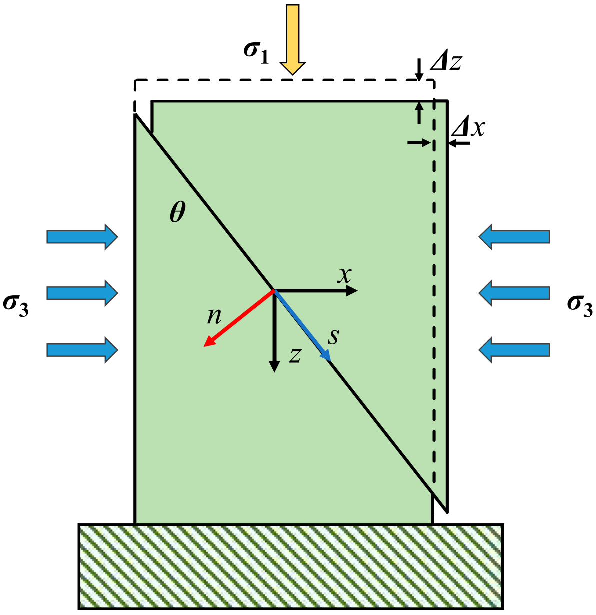

FIGURE 3
Schematic view of sample deformation during the slip process (after Ye and Ghassemi, 2018).

stress, surface roughness, and critical shear stress on the slip behavior were explored. Their results showed that the fracture stability during the slipping process was controlled by the relative magnitude between system stiffness and fracture weakening rate. And an empirical formula was proposed for predicting the released seismic moment. To explore the coupling hydro-mechanical effect on the slip and activation processes of fracture, Ye and Ghassemi (2018), Ye and Ghassemi (2020) carried out triaxial injection-induced shear tests on the rough fracture. They found that when the fractures were activated, the fractures may enter the quasi-static slip stage firstly, and eventually enter the dynamic slip stage. The heterogeneously distributed acoustic emission activities accompanied by the occurrence of dynamic slip were also observed. Wang et al. (2020) studied fracture slip behavior by changing fluid pressurization rate and injection pressure, and the results show that fault creep was more significantly controlled by the fluid pressurization rate comparing with injection pressure. Additionally, Zeng et al. (2022) focused on the effects of pH, viscosity and bentonite particles on the shear slip mechanism of shale formation. They concluded that the instability of shale fractures may be more likely to occur for larger pH, viscosity and the bentonite content. In the process of unconventional resource exploitation, the drilling process and continuous extraction of shale gas lead to the reduction in confining pressure on the natural fractures (Yin et al., 2015; Zhou et al., 2019; Liu et al., 2024). Therefore, it is imperative to study the effects of unloading rate of confining pressure on the slip behavior of fracture.

The shale rock shows obvious heterogeneity, discontinuity, and anisotropy, which can be manifested in two parameters, i.e., the strike and the inclination angle (Mohammadi and Pietruszczak, 2019; Latyshev and Prishchepa, 2020; Huang et al., 2021; Yang et al., 2023). The effects of strike and the inclination angle on the mechanical characteristics of rock were studied by some scholars (Duan et al., 2023; Zhu et al., 2022). Duan et al. (2023) studied the effects of fracture dip angle and fracture length on the propagation of cracks through a similar simulation test and RFPA2D-dynamic numerical simulation software. They concluded that with the increase in the inclination angle, the number of secondary cracks increased and the enhancement of permeability was strengthened. Similar phenomenon was also observed by Liu et al. (2023). Ma and Wang (2020) numerically explored the influence of inclination angle on the failure modes of rock mass. Their results showed that the increment of inclination angle led to the failure modes changed from brittle failure to ductile failure. Previous studies mostly focused on the influence of inclination angle on the failure modes of rock mass, and few studies have considered the influence of fracture inclination angle on activation and slipping process of fracture. Consequently, it is necessary to explore the combined effects of inclination angle and unloading rate of confining pressure on the slip behaviors of fractures.

In this study, the saw-cut shale fractures with different inclination angles were prepared for the unloading-induced slip experiments. The fractures were firstly driven to the critical stress state, and then the confining pressure was step unloaded at two different rates until the fractures were activated. The effect of unloading rate of confining pressure and inclination angle on the mechanical response, slipping process, and frictional behavior of fractures were systematically explored. The variation in the morphology and the joint roughness coefficient were investigated. Our results may shed light on the seismicity mitigation and safe exploitation of shale gas.

2 Materials and methods

2.1 Sample preparation and experimental setup

The shale samples were collected from the Longmaxi shale outcrops in the Sichuan Basin, China. X-ray diffraction (XRD) results indicate that the main mineral compositions of shale samples are quartz, calcite, and illite, which account for 38.7%, 18.2%, and 17.6%, respectively. As shown in Figure 1, two sets of samples with different inclination angles θ (i.e., θ = 30° and 50°) of saw-cutting fractures were prepared from the cylindrical shale cores. And each set contains two shale fracture samples with the same θ. The length and diameter of all shale cores are 100 and 50 mm, respectively. In order to avoid the generation of new cracks in rock matrix, the θ used in the experiments should lie between 20° and 55° (Brady and Brown, 2006; Ji et al., 2022). Thus, the fractures with θ = 30° and 50° were adopted in this study.

The experiments were conducted using the MTS 815 rock mechanic testing system equipped with servocontrolled confining pressure system and triaxial system (see Figure 2). Figure 3 demonstrates the triaxial stress state of samples and sample deformation during the slip process. The differential stress $\sigma_1 - \sigma_3$ was loaded by the axil piston, and the confining pressure σ_3 was pressurized by injecting the hydraulic oil into the triaxial chamber (Passelègue et al., 2018). The normal stress σ_n and shear stress τ acting on the saw-cutting fracture can be attained by

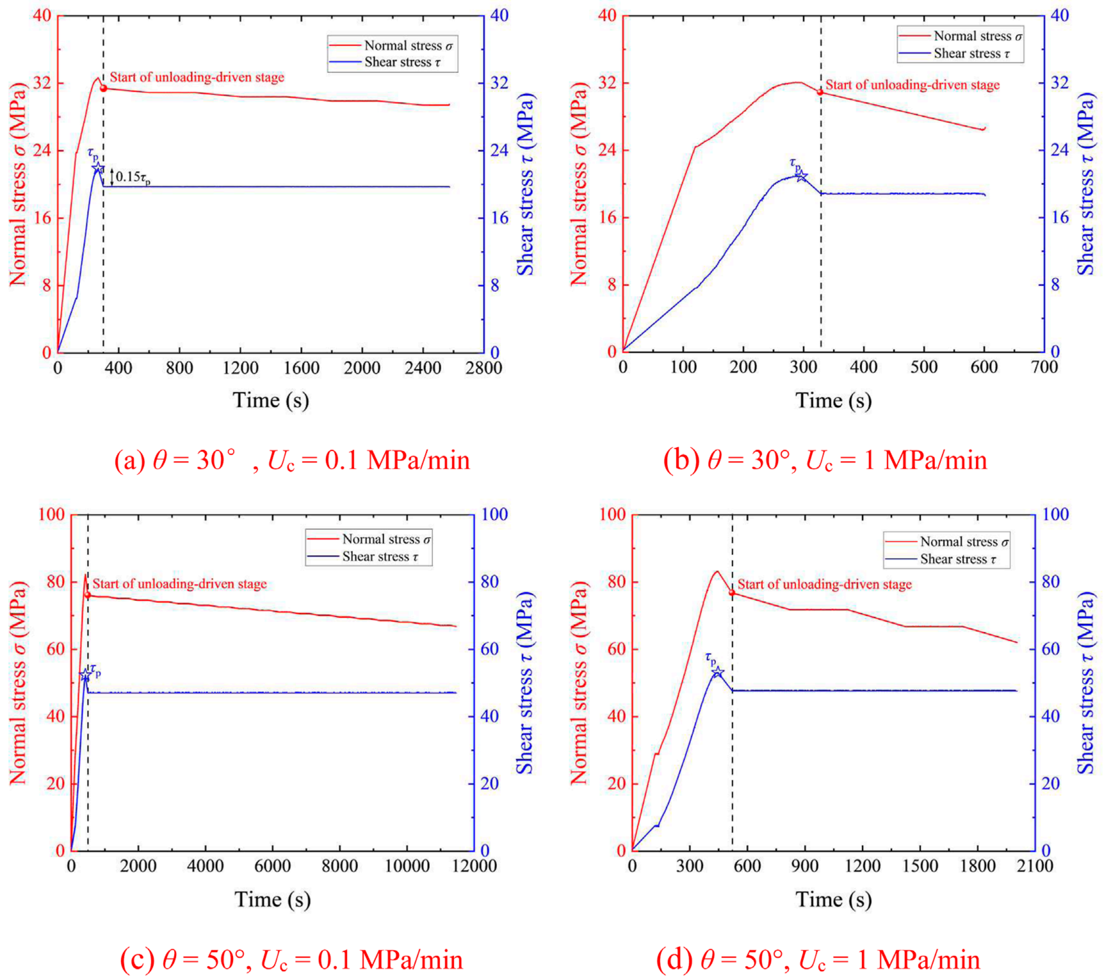

FIGURE 4
Evolutions of normal and shear stresses during the slip process under different unloading rates of confining pressure Uc for the fractures with θ = 30° and θ = 50°. **(A)** θ = 30°, Uc = 0.1 MPa/min **(B)** θ = 30°, Uc = 1 MPa/min **(C)** θ = 50°, Uc = 0.1 MPa/min **(D)** θ = 50°, Uc = 1 MPa/min.

Zhu et al. (2023):

$$\tau = (\sigma_1 - \sigma_3)\sin\theta\cos\theta \tag{1}$$

$$\sigma_n = \sigma_3 + (\sigma_1 - \sigma_3)\sin^2\theta \tag{2}$$

where σ_1 is the axial stress, equaling to the sum of $\sigma_1 - \sigma_3$ and σ_3. For a given θ, the σ_n and τ can be well controlled by adjusting the $\sigma_1 - \sigma_3$ and σ_3. The axial displacement Δz and radial displacement Δx of the sample were measured using the internal sensor embedded in the piston and circumferential extensometer, respectively. The upper part of the sample tended to slip along the facture surface, so the coordinate transformation of the displacement is necessary. The shear displacement d_s along the shear direction can be calculated as Equation 3, Ye and Ghassemi (2018):

$$d_s = \Delta z\cos\theta + \Delta x\sin\theta \tag{3}$$

Throughout the experiment, the $\sigma_1 - \sigma_3$, σ_3, Δx, and Δz were all synchronously recorded with a sampling rate of 1HZ. The fracture surfaces were scanned before and after experiments using the three-dimensional scanning system 3DSS for the characterization of the morphology (Liu et al., 2024).

2.2 Experimental procedures

The triaxial unloading-induced slip experiment consists of displacement-driven stage and unloading-driven slipping stage. In the displacement-driven stage, the σ_3 was firstly loaded to 20 MPa with a loading rate of 10 MPa/min and then held constant during this stage. At the same time, the piston moved downward slowly to load the $\sigma_1 - \sigma_3$ until the peak shear strength τ_p was reached. The gentle loading process of $\sigma_1 - \sigma_3$ can effectively avoid the early activation of fracture at this stage (Ji et al., 2023). Then, the piston moved upward, and the $\sigma_1 - \sigma_3$ decreased. The τ applied on the fracture was reduced slowly to $0.85\tau_p$, and the fracture was considered to be in the critical stress state. In the unloading-driven stage, the $\sigma_1 - \sigma_3$ was kept constant, and the σ_3 was step unloaded.

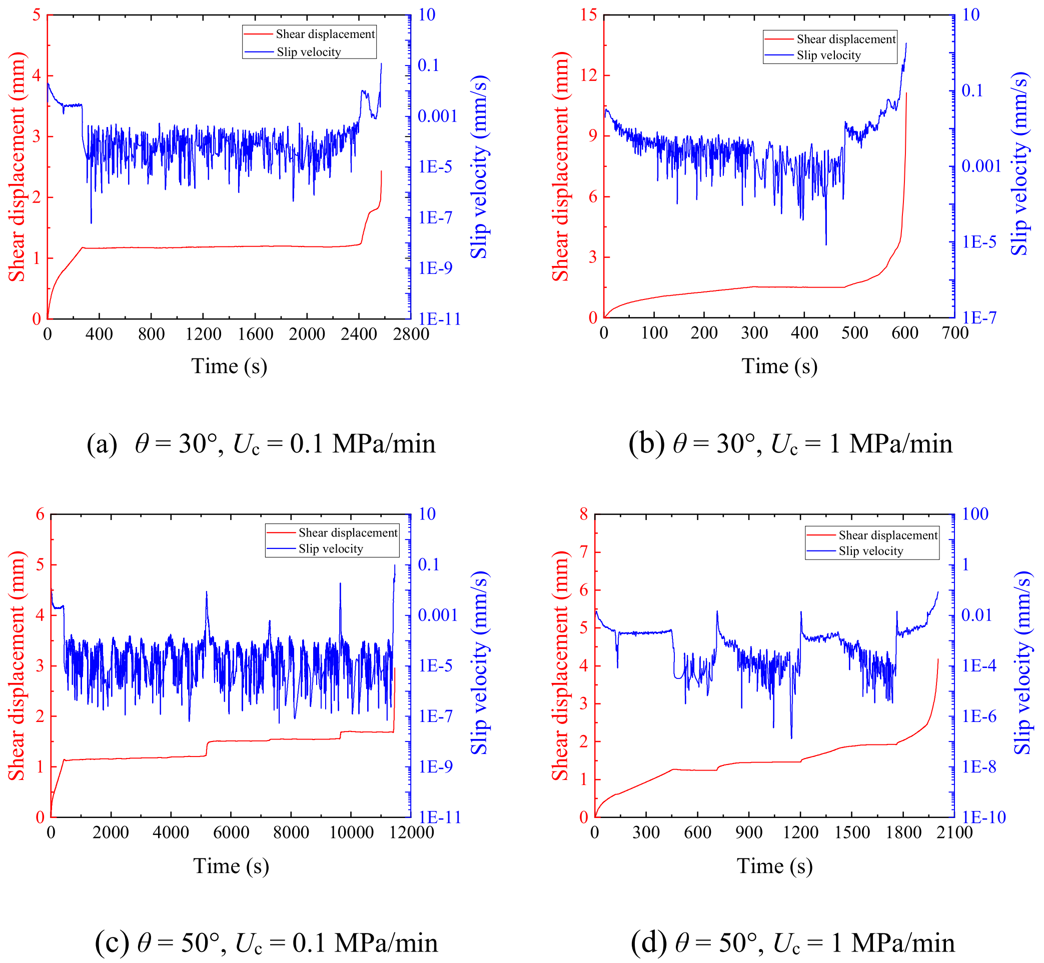

FIGURE 5
Evolutions of kinematic parameters during the slip process under different Uc for the fractures with θ = 30° and θ = 50°. **(A)** θ = 30°, Uc = 0.1 MPa/min **(B)** θ = 30°, Uc = 1 MPa/min **(C)** θ = 50°, Uc = 0.1 MPa/min **(D)** θ = 50°, Uc = 1 MPa/min.

According to Equations 1, 2, the τ was held constant, while the σ_n was step unloaded at the same rate as the σ_3. During this stage, the σ_3 was unloaded with an unloading rate U_c (i.e., 0.1 MPa/min and 1 MPa/min) for 5 min, and then σ_3 was held constant for another 5 min. After that, the σ_3 was unloaded for 5 min and maintained constant for 5 min again. This process was repeated until the fracture was activated.

Hydraulic fracturing with stepwise pressurization is widely used in shale gas exploitation to enhance reservoir permeability (Gehne and Benson, 2019; Parchei-Esfahani et al., 2020; Xu et al., 2022). The probability of fracture activation and the released seismic moment can be significantly reduced by stepwise pressurization (Passelègue et al., 2018; Wang et al., 2020; Liu et al., 2024). Based on the Terzaghi effective stress principle, with the step increase in pore pressure, the effective normal stress applied on the fractures decreases step by step (Lade and De Boer, 1997). The stepwise pressurization is equivalent to the step unloading of confining pressure in the triaxial unloading-induced slip experiments, as well as the effective normal stress (i.e., σ_n in our study).

3 Results and analysis

3.1 Mechanical stability of fractures

Figure 4 shows the evolutions of σ_n and τ during the experiments under different U_c for the fractures with $\theta = 30°$ and θ = 50°. In the displacement-driven stage, both of the σ_n and τ gradually increased. The increasing rate of σ_n was always larger than that of τ in the first 2 minutes. After that, due to the maintaining of σ_3, the σ_n and τ increased at the same rate and reached the peak values. The θ has great influence on the τ_p. For the fracture with $\theta = 30°$, the mean value of τ_p was 21.37 MPa. While for $\theta = 50°$, the mean value of τ_p was 52.59 MPa, which is 2.46 times larger than that of $\theta = 30°$. The τ_p was significantly enhanced due to the increase in θ. At the end of displacement-driven stage, both of the σ_n and τ decreased. In the unloading-driven stage, the τ was held constant, while the σ_n was step decreased at the same rate as the σ_3.

The evolutions of kinematic parameters during the slip process under different U_c for the fractures with $\theta = 30°$ and $\theta = 50°$ were

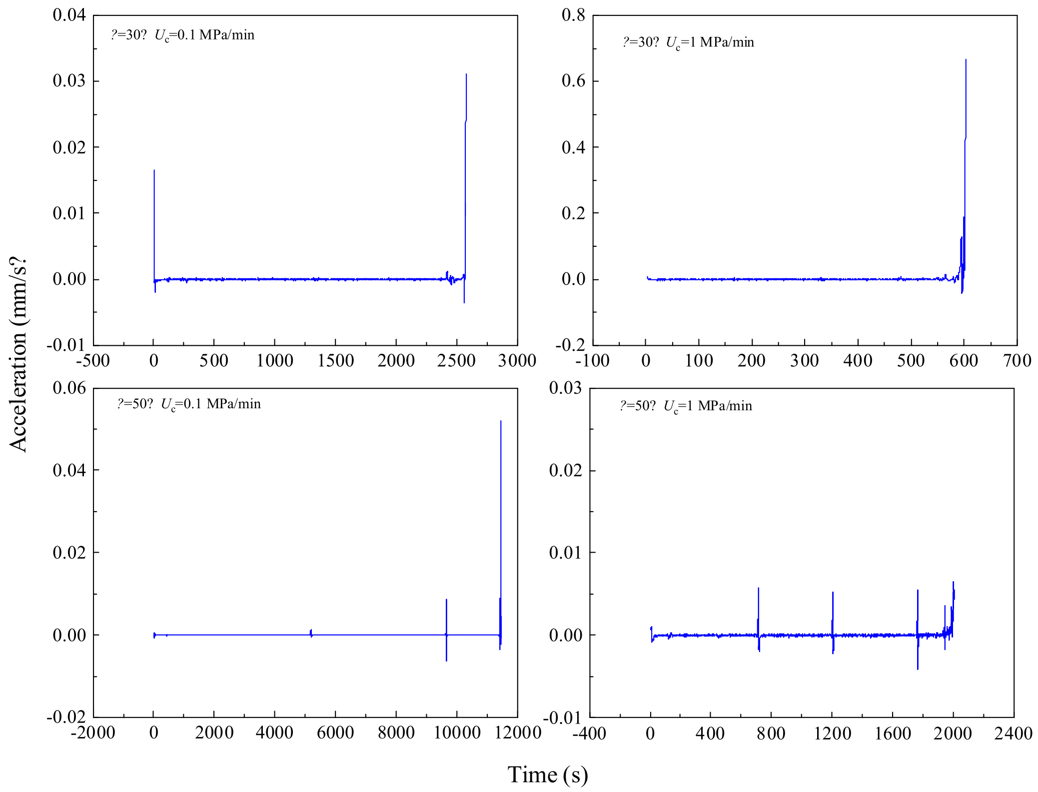

FIGURE 6
Variation in acceleration during the slip process for the fractures under different Uc with θ = 30° and 50°.

shown in Figure 5. Because the variation in shear displacement was induced by the manually controlled loading process of $\sigma_1 - \sigma_3$, thus, we focused on the slipping behavior of fractures in the unloading-driven stage. At the beginning of unloading-driven stage, the fractures remained stable state with slight fluctuation of slip velocity. With continuous unloading of σ_3, the decreasing of σ_3 as perturbation during the unloading process broke the initially stable stress state of the fractures. The fractures were activated and eventually entered the dynamic slip stage. We defined that the activation point was the time point when the fracture slip velocity was greater than 0.003 mm/s, and the dynamic slip stage began when the fracture slip velocity was greater than 0.1 mm/s (Wang et al., 2020; Liu et al., 2023). For example, for the fracture with θ = 50° under U_c = 1 MPa/min, the fracture was activated to slip at t = 712.53 s and finally entered the dynamic slip stage at t = 2005.20 s. At the onset of dynamic slip stage, the shear displacement, slip velocity and acceleration dramatically increased. The phase between activation point and the onset of dynamic slip stage was defined as the quasi-static slip stage (Liu et al., 2023). It can be observed that three times of sharp increase in slip velocity and acceleration occurred during the quasi-static slip stage (see Figure 6), which were referred as stick-slip events (Ji et al., 2019; Wang et al., 2020). The stick-slip is characterized by an event with a peak acceleration larger than 0.005 mm/s^2, commonly accompanied by the sharp drop in shear stress (Leeman et al., 2018; Liu et al., 2024).

The slip behaviors of fractures were greatly affected by U_c and θ. There was a distinguished trend of the number of stick-slip events (see Figure 7A, B). As U_c increased from 0.1 to 1 MPa/min, the stick-slip events occurred from 0 to 1 time for θ = 30°, while that kept constant for θ = 50°. For the fractures with θ = 50°, the duration of quasi-static slip stage for the fracture under U_c = 0.1 MPa/min was 4.8 times longer than that under U_c = 1 MPa/min. The reasons may be that due to the lower U_c, the asperities on fracture surfaces can have more time to self-stabilize by releasing the strain energy slowly instead the asperities were sheared-off suddenly. Therefore, the occurrence of dynamic slip stage under U_c = 0.1 MPa/min was latter than that under U_c = 1 MPa/min. And with the increase in θ, the generated shear displacement during the quasi-static slip stage increased. As the θ increased from 30° to 50°, the generated shear displacement increased from 0.077 to 2.357 mm under U_c = 0.1 MPa/min and from 0.398 to 1.837 mm under U_c = 1 MPa/min, respectively. Figure 8A shows the variation in peak shear strength for different fractures, and Figures 8B, C show the evolutions of τ and σn applied on the fracture at the activation point and the onset of dynamic slip stage, respectively. With increasing θ, both τ and σ_n significantly increased at the activation point and the onset of dynamic slip stage. And the θ has greater influence on the stress state of fracture than that of U_c. As the increased from 30° to 50°, the τ at the activation point increased from 19.73 to 47.04 MPa under U_c = 0.1 MPa/min, while under U_c = 1 MPa/min, the τ increased from 18.81 to 47.63 MPa.

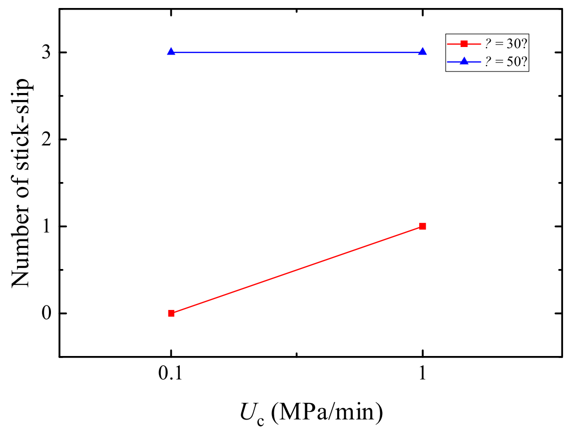

(a) Variation in the number of stick-slip events

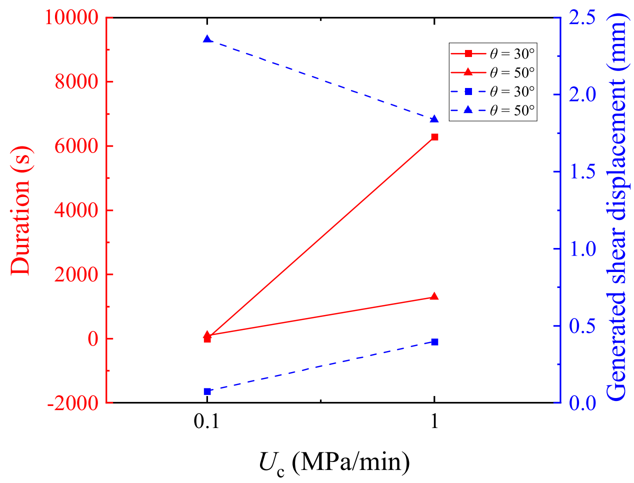

(b) Duration and generated shear displacement for fractures under different U_c

FIGURE 7
Number of stick-slip events, the duration, and the generated shear displacement during the quasi-static slip stage for fractures under different Uc. **(A)** Variation in the number of stick-slip events. **(B)** Duration and generated shear displacement for fractures under different Uc.

3.2 Frictional characteristics of fractures

The friction coefficient is defined as the ratio of τ to σ_n, which has been widely adopted for characterizing the stability of fracture (Doglioni, 2018; Liu et al., 2023; Moein et al., 2023). Figure 9 shows the variation in μ with shear displacement d_s under different θ and U_c. And the μ_s and μ_{ss} represent the friction coefficient when the peak shear strength was reached and the dynamic slip occurred for each fracture, respectively. In the start of displacement-driven stage, the increment of σ_3 was larger than that of $\sigma_1 - \sigma_3$, leading to the quick decrease in μ. Then, the σ_3 was held constant, the continuous loading of $\sigma_1 - \sigma_3$ resulted in the rapid increase in μ until the μ_s was reached. At the end of displacement-driven stage, to make the fracture close to the critical stress state, the $\sigma_1 - \sigma_3$ was slowly decreased. The μ met a slow decrease, and the rebound of shear displacement was also observed. In the unloading-driven stage, the $\sigma_1 - \sigma_3$ was maintained, and the σ_3 was step unloaded. Thus, the μ slowly increased and eventually reached the μ_{ss} at the onset of dynamic slip.

The evolutions of μ_s and μ_{ss} for the fractures with different θ under different U_c were shown in Figures 9A, B. As the U_c increased from 0.1 to 1 MPa/min, both μ_s and μ_{ss} decreased significantly for the fractures with θ = 30°. However, for the fractures with θ = 50°, with increasing U_c, the μ_s and μ_{ss} met slight increase. As the U_c increased from 0.1 to 1 MPa/min, the μ_s and μ_{ss} varied from 0.635 to 0.637 with a strengthening rate of 0.31%, and from 0.703 to 0.768 with a strengthening rate of 9.25%, respectively (see Figure 10). It means that the increasing θ weakened the weakening effect of

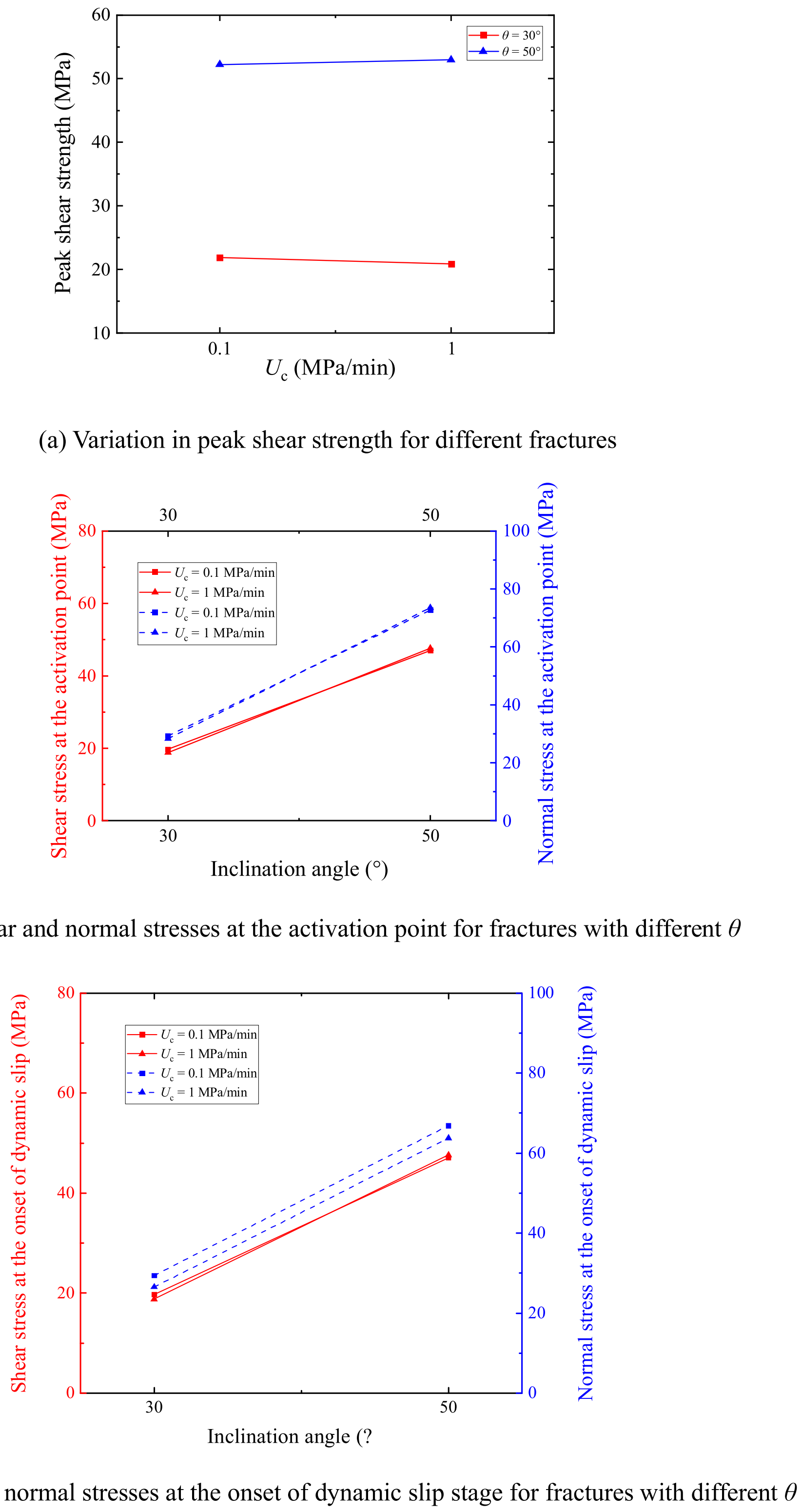

FIGURE 8
Stress state for fractures under different Uc with different θ at the activation point and at the onset of dynamic slip stage. **(A)** Variation in peak shear strength for different fractures. **(B)** Shear and normal stresses at the activation point for fractures with different θ. **(C)** Shear and normal stresses at the onset of dynamic slip stage for fractures with different θ.

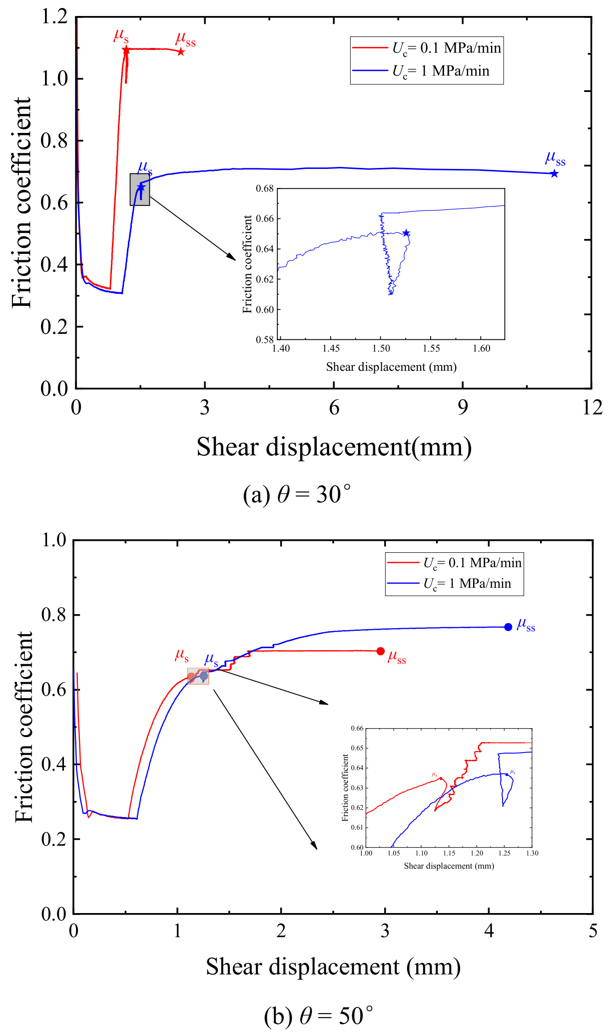

FIGURE 9
Friction coefficient versus shear displacement for the fractures with different θ. Here, μs and μss represent the friction coefficient when the peak shear strength was reached and the dynamic slip occurred for each fracture, respectively. **(A)** θ = 30°. **(B)** θ = 50°.

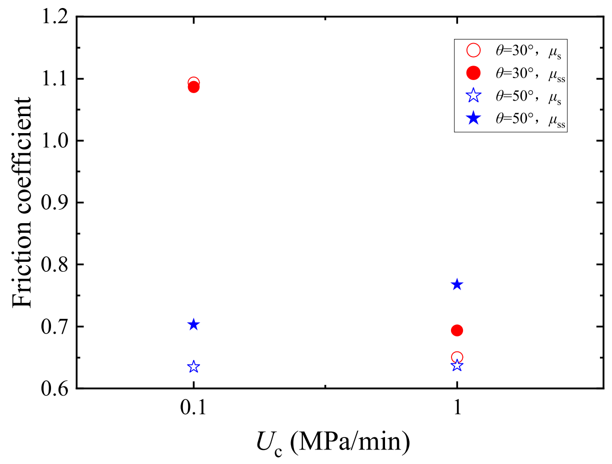

FIGURE 10
Evolutions of μs and μss for the fractures with different θ under different Uc.

the U_c on the μ_s and μ_{ss}. This implies that there is a competitive relationship between the θ and U_c for the evolution of the frictional behavior of fractures. The μ_s and μ_{ss} of most fractures range from 0.6 to 0.8, aligning with the Byerlee's law proposed by Byerlee (1978), Giorgetti et al. (2019), Yin et al. (2024).

3.3 Variations in morphology

Figure 11 shows the morphologies of fracture surfaces with θ = 30° and 50° under different U_c before and after experiments. Before experiments, the fracture surfaces were filled with asperities despite being saw-cut and polished. After experiments, the asperities were partially damaged to a certain degree and the elevation of fracture surfaces generally decreased, with respect to the morphology images before the experiments. The damage of fracture surfaces can be obviously recognized that was deeper at end of the fractures than that of other regions. The method recommended by the International Society of Rock Mechanics and Engineering, joint roughness coefficient (JRC) was used, so as to assess the quantification of fracture surface roughness, which are estimated by Equations 4, 5 Ji et al. (2023), Liu et al. (2023), Zhu et al. (2024):

$$Z_2 = \left[\frac{1}{N} \sum \left(\frac{z_{i-1} - z_i}{y_{i-1} - y_i} \right)^2 \right]^{1/2} \tag{4}$$

$$\text{JRC} = 32.2 + 32.47\log Z_2 \tag{5}$$

where Z_2 is the root mean square of the first derivative of the measuring line, N is the number of the sample points in the measuring lines, z_i and y_i are the coordinate of each sample point. Many studies have manifested that the JRC is anisotropic and has great influence on the morphology, quantity and spatial distribution characteristics of fractures (Tian et al., 2022; Soomro et al., 2022; Liu et al., 2023; Adnan et al., 2023). The JRC is calculated by setting measuring lines on the fracture surfaces and appraising the elevation fluctuation of adjacent points, so JRC at different directions has central symmetry (Liu et al., 2024). In our experiments, it is assumed that the angle along the positive direction of the y-axis is 0°. The JRC of the fractures under different θ and U_c was calculated in six directions along the counterclockwise direction (i.e., 0°, 30°, 60°, 90°, 120° and 150°).

The directional JRC contours of four fracture surfaces before and after experiments were plotted in Figure 12, which illustrates the changes of JRC in all directions clearly. The JRC approaching the x-axis direction increased a lot due to the generation of scratches, which can be linked with the occurrence of stick-slip events. During the slipping process, the asperities on the upper and lower fracture surfaces were interlaced and then sheared-off along the y direction or the shearing direction. Under different U_c, the characteristics of the variation in JRC were presented in Figure 12. When U_c = 0.1 MPa/min, the JRC along the directions of 0° and 90° were 5.93 and 5.76 for the fractures with θ = 30°, 5.14 and 5.20 for the fractures

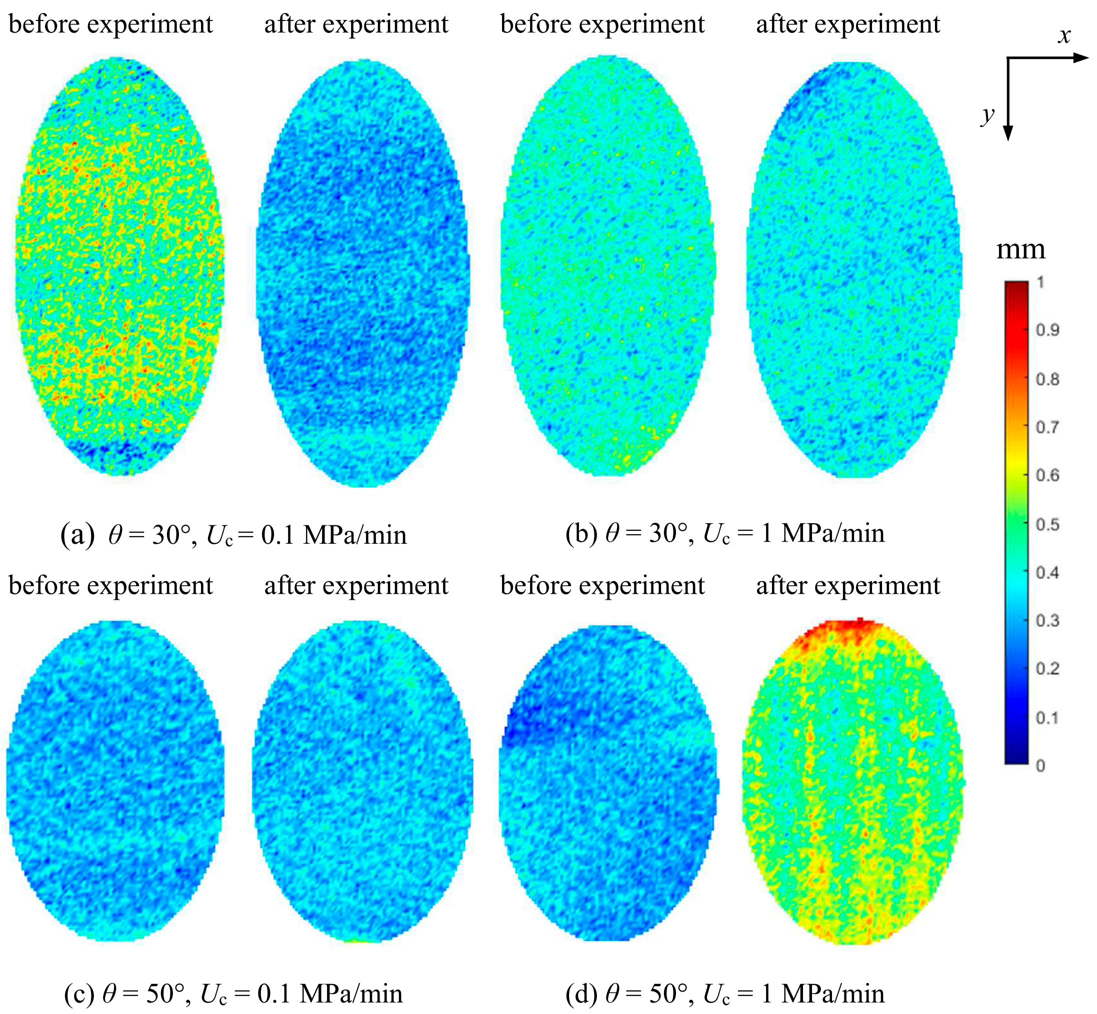

FIGURE 11
Morphologies of fracture surfaces with θ = 30° and 50° under different Uc before and after experiments. **(A)** θ = 30°, Uc = 0.1 MPa/min **(B)** θ = 30°, Uc = 1 MPa/min **(C)** θ = 50°, Uc = 0.1 MPa/min **(D)** θ = 50°, Uc = 1 MPa/min.

with θ = 50°, respectively. As U_c increased from 0.1 to 1 MPa/min, the ratio of the calculated JRC along the 0° and 90° descended slightly for both θ = 30° and 50°, from 1.03 to 1.00 and from 0.99 to 0.98 for the fracture surfaces after experiments, respectively. Due to the generation of scratches, the average JRC value JRC_{ave} of most fracture surfaces increased after the experiment, except for fracture with θ = 50° and U_c = 0.1 MPa/min (see Figure 13). As shown in Figure 14, the variation in the ratio of the maximum of the directional JRC (JRC_{max}) to the minimum of the directional JRC (JRC_{min}) with varying the U_c, can explain that JRC has anisotropy. When the U_c increased from 0.1 to 1 MPa/min, the value of JRC_{max}/JRC_{min} for the fractures before and after experiments decreased from 1.03 to 0.94 with θ = 30°, and increased from 1.05 to 1.09 with θ = 50°. It may be caused by the crushing and damage of the asperities during the slipping process. Some scholars found that a large amount of energy is radiated due to the damage of fracture asperities, accompanied by a rapid increase in acoustic emission events (Wang et al., 2020; Lin et al., 2021; Lin et al., 2024; Guérin-Marthe et al., 2023).

4 Conclusion

In this study, the effects of inclination angle θ and unloading rate of confining pressure U_c on the mechanical response, slipping process, and frictional behavior were studied by conducting triaxial unloading-induced fracture slip experiments. The variation in the morphology and the joint roughness coefficient were investigated. Our experimental results show that with the continuous unloading of confining pressure, the fractures were initiated to slip, then entered the quasi-static slip stage, and eventually entered the dynamic slip stage in sequence. The occurrence of stick-slip events in the quasi-static slip stage was strongly influenced by the θ and U_c. With increasing θ and U_c, the number of stick-slip events increased a lot. As the θ increased from 30° to 50°, the stick-slip events occurred from 0 to 3 times and from 1 to 3 times for U_c = 0.1 and 1 MPa/min, respectively. The duration of quasi-static slip stage for the fracture with θ = 50° under U_c = 0.1 MPa/min was 4.8 times longer than that under U_c = 1 MPa/min. And the increase in θ promotes the slip process of fracture and the shear displacement generated during

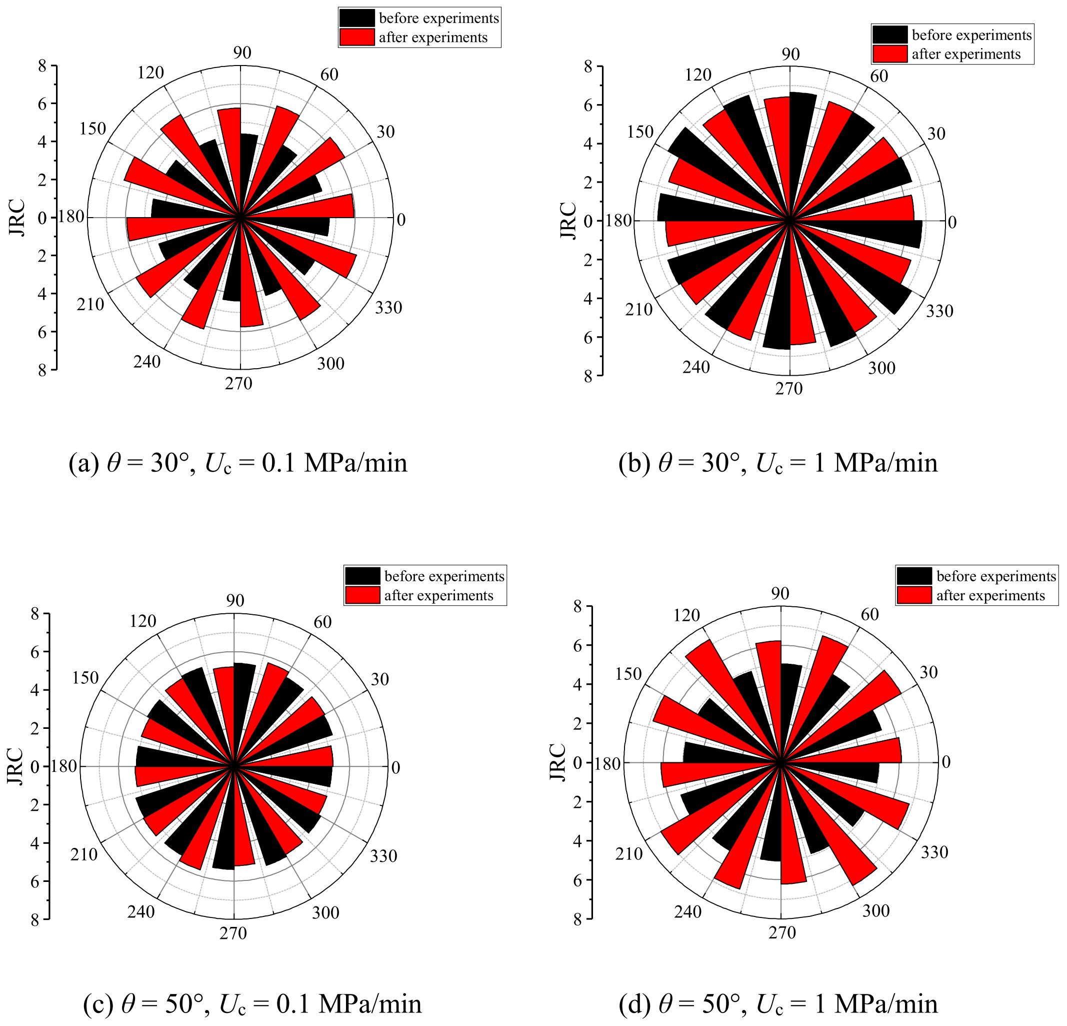

FIGURE 12
Directional joint roughness coefficient (JRC) contours of fracture surfaces before and after experiments. **(A)** θ = 30°, Uc = 0.1 MPa/min **(B)** θ = 30°, Uc = 1 MPa/min **(C)** θ = 50°, Uc = 0.1 MPa/min. **(D)** θ = 50°, Uc = 1 MPa/min.

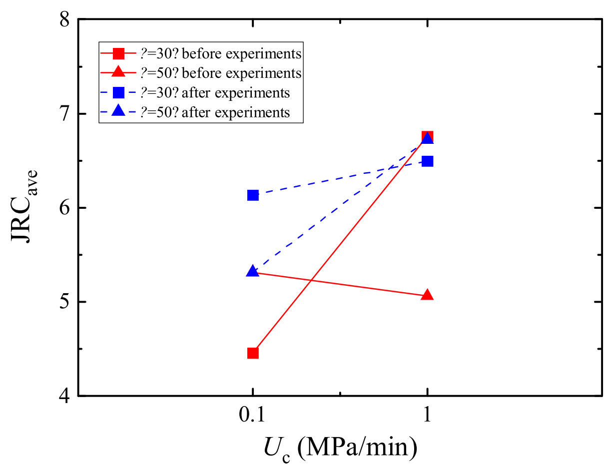

FIGURE 13
Effects of θ and Uc on the evolutions of average JRC value (JRCave) before and after the experiments.

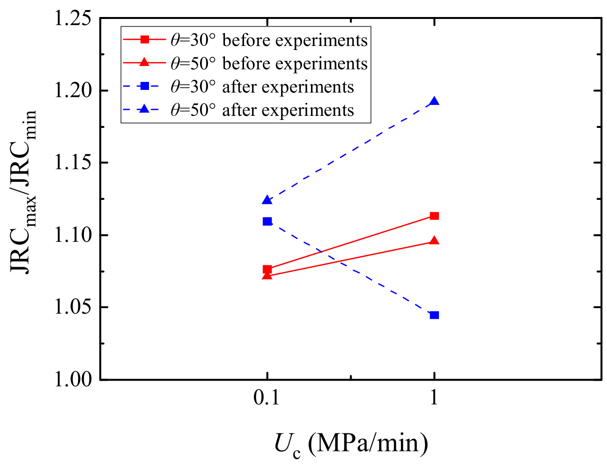

FIGURE 14
Effects of θ and Uc on the evolutions of JRCmax/JRCmin before and after the experiments. Here, JRCmax represents the maximum JRC in the directional JRC contours, while JRCmin represents the minimum JRC in the directional JRC contours.

the quasi-static slip stage increased significantly. With increasing θ, both shear stress τ and normal stress σ_n greatly increased at the activation point and the onset of dynamic slip stage. The θ and U_c have a great influence on the interaction mode between the fractures, which directly affects the friction properties of the fractures. With the increment of θ, the σ_n applied on fractures shows a downward trend. Therefore, the interaction form between asperities during the slip process may be changed into non-tight contact stage. As the U_c increased from 0.1 to 1 MPa/min, both the friction coefficient when the peak shear strength was reached μ_s and the dynamic slip occurred μ_{ss} decreased significantly for the fractures with θ = 30°. For the fractures with θ = 50°, the μ_s and μ_{ss} increased with different strengthening rate, which varied from 0.635 to 0.637 with a strengthening rate of 0.31% for U_c = 0.1 MPa/min, and from 0.703 to 0.768 with a strengthening rate of 9.25% for U_c = 1 MPa/min, respectively. The increase in θ may enhance or impair the anisotropy of JRC, depending on whether the U_c reached a certain rate between 0.1 MPa/min and 1 MPa/min. Our results may enrich the potential mechanism of fracture activation in existing literatures and shed light on the seismicity mitigation and safe exploitation of shale gas.

In the future, our studies will focus on the slip characteristics of shale fractures by more sets of inclination angles and unloading rates of confining pressure to study the equilibrium point of their competitive relationships. The mechanical and hydraulic fully coupling effect on the slip behavior and moment release will also be concerned in the future works. Thus, the implementation of triaxial injection-induced fracture slip experiments is necessary. The radiated seismic energy (e.g., acoustic emission events) during the slip process of fracture should also be monitored in real time, and the positioning of AE hypocenters is essential. The temporal evolution of AE sources should be correlated with the slip characteristics and damage modes of fractures, which will further clarify the mechanism of shale fracture activation in the future studies.

Data availability statement

The original contributions presented in the study are included in the article/supplementary material, further inquiries can be directed to the corresponding author.

Author contributions

ZY: Writing–original draft, Writing–review and editing. YC: Writing–original draft, Writing–review and editing. TZ: Writing–original draft, Writing–review and editing. SL: Writing–original draft, Writing–review and editing. XF: Writing–original draft, Writing–review and editing.

Funding

The author(s) declare that no financial support was received for the research, authorship, and/or publication of this article.

Conflict of interest

The authors declare that the research was conducted in the absence of any commercial or financial relationships that could be construed as a potential conflict of interest.

Publisher's note

References

Adnan, R. R., Ismail, M. M., Yusoff, I. N., Tobe, H., Miyoshi, T., Date, K., et al. (2023). Preliminary assessment of joint roughness coefficient of rock slope using close-range photogrammetry technique. *Phys. Chem. Earth* 130, 103347. doi:10.1016/j.pce.2022.103347

Bourne, S. J., Oates, S. J., and Van Elk, J. (2018). The exponential rise of induced seismicity with increasing stress levels in the Groningen gas field and its implications for controlling seismic risk. *Geophys. J. Int.* 213 (3), 1693–1700. doi:10.1093/gji/ggy084

Brady, B. H. G., and Brown, E. T. (2006). *Rock mechanics: for underground mining*. Springer science and business media.

Byerlee, J. (1978). Friction of rocks. *Pure and Applied Geophysics PAGEOPH* 116 (4-5), 615–626. doi:10.1007/BF00876528

Cao, H., Wang, T., Bao, T., Sun, P., Zhang, Z., and Wu, J. (2018). Effective exploitation potential of shale gas from lower cambrian niutitang formation, Northwestern Hunan, China. *Energies* 11 (12), 3373. doi:10.3390/en11123373

Doglioni, C. (2018). A classification of induced seismicity. *Geosci. Front.* 9 (6), 1903–1909. doi:10.1016/j.gsf.2017.11.015

Duan, D., Chen, X., Feng, X., Liu, W., Zhang, H., Chen, X., et al. (2023). Influence of joint characteristics on crack propagation during the double-hole high-energy gas impact permeability enhancement process. *Sustainability* 14 (24), 16342. doi:10.3390/su142416342

Eshiet, K. I. I., and Sheng, Y. (2017). The role of rock joint frictional strength in the containment of fracture propagation. *Acta Geotech.* 12 (4), 897–920. doi:10.1007/s11440-016-0512-2

Feng, F., Chen, S., Wang, Y., Huang, W., and Han, Z. (2021). Cracking mechanism and strength criteria evaluation of granite affected by intermediate principal stresses subjected to unloading stress state. *Int. J. Rock Mech. Min. Sci.* 143, 104783. doi:10.1016/j.ijrmms.2021.104783

Gehne, S., and Benson, P. M. (2019). Permeability enhancement through hydraulic fracturing: laboratory measurements combining a 3D printed jacket and pore fluid over-pressure. *Sci. Rep.* 9 (1), 12573. doi:10.1038/s41598-019-49093-1

Giorgetti, C., Tesei, T., Scuderi, M. M., and Collettini, C. (2019). Experimental insights into fault reactivation in gouge-filled fault zones. *J. Geophys. Res. Solid Earth* 124 (4), 4189–4204. doi:10.1029/2018jb016813

Guérin-Marthe, S., Kwiatek, G., Wang, L., Bonnelye, A., Martínez-Garzón, P., and Dresen, G. (2023). Preparatory slip in laboratory faults: effects of roughness and load point velocity. *J. Geophys. Res. Solid Earth* 128 (4), e2022JB025511. doi:10.1029/2022jb025511

He, M., Zhao, F., Du, S., and Zheng, M. (2014). Rockburst characteristics based on experimental tests under different unloading rates. *Rock Soil Mech.* 35 (10), 2737–2747. doi:10.16285/j.rsm.2014.10.001

Hou, L., Luo, X., Yu, Z., Wu, S., Zhao, Z., and Lin, S. (2021). Key factors controlling the occurrence of shale oil and gas in the Eagle Ford Shale, the Gulf Coast Basin: models for sweet spot identification. *J. Nat. Gas Sci. Eng.* 94, 104063. doi:10.1016/j.jngse.2021.104063

Hu, T., Pang, X., Jiang, F. J., Wang, Q., Liu, X., Wang, Z., et al. (2021). Movable oil content evaluation of lacustrine organic-rich shales: methods and a novel quantitative evaluation model. *Earth Sci. Rev.* 214, 103545. doi:10.1016/j.earscirev.2021.103545

Huang, N., Liu, R., Jiang, Y., and Cheng, Y. (2021). Development and application of three-dimensional discrete fracture network modeling approach for fluid flow in fractured rock masses. *J. Nat. Gas Sci. Eng.* 91, 103957. doi:10.1016/j.jngse.2021.103957

Ji, H., Liu, R., Yu, L., and Zhu, X. (2023). Influence of joint inclination on mechanical behaviors of shales during unloading-induced slip processes. *Int. J. Rock Mech. Min. Sci.* 170, 105487. doi:10.1016/j.ijrmms.2023.105487

Ji, Y., Wu, W., and Zhao, Z. (2019). Unloading-induced rock fracture activation and maximum seismic moment prediction. *Eng. Geol.* 262, 105352. doi:10.1016/j.enggeo.2019.105352

Ji, Y., Hofmann, H., Rutter, E. H., Xiao, F., and Yang, L. (2022). Revisiting the evaluation of hydraulic transmissivity of elliptical rock fractures in triaxial shear-flow experiments. *Rock Mech Rock Eng.* 55, 3781–3789. doi:10.1007/s00603-022-02797-9

Kivi, I. R., Pujades, E., Rutqvist, J., and Vilarrasa, V. (2022). Cooling-induced reactivation of distant faults during long-term geothermal energy production in hot sedimentary aquifers. *Sci. Rep.* 12 (1), 2065. doi:10.1038/s41598-022-06067-0

Lade, P. V., and De Boer, R. (1997). The concept of effective stress for soil, concrete and rock. *Geotechnique* 47 (1), 61–78. doi:10.1680/geot.1997.47.1.61

Langenbruch, C., and Zoback, M. D. (2016). How will induced seismicity in Oklahoma respond to decreased saltwater injection rates? *Sci. Adv.* 2 (11), e1601542. doi:10.1126/sciadv.1601542

Latyshev, O. G., and Prishechepa, D. V. (2020). Fractured rock mass modeling and stress–strain analysis using the finite element method. *Phys. Rocks Process.* 10, 17580. doi:10.17580/gzh.2020.05.01

Leeman, J. R., Marone, C., and Saffer, D. M. (2018). Frictional mechanics of slow earthquakes. *J. Geophys. Res. Solid Earth* 123 (9), 7931–7949. doi:10.1029/2018jb015768

Lei, Q., Weng, D., Guan, B., Shi, J., Cai, B., He, C., et al. (2023). Shale oil and gas exploitation in China: technical comparison with US and development suggestions. *Petroleum Explor. Dev.* 50 (4), 944–954. doi:10.1016/s1876-3804(23)60440-9

Lei, X., Huang, D., Su, J., Jiang, G., Wang, X., Wang, H., et al. (2017). Fault reactivation and earthquakes with magnitudes of up to Mw4.7 induced by shale-gas hydraulic fracturing in Sichuan Basin, China. *Sci. Rep.* 7 (1), 7971. doi:10.1038/s41598-017-08557-y

Lei, X., Wang, Z., and Su, J. (2019). The December 2018 ML 5.7 and January 2019 ML 5.3 earthquakes in south Sichuan Basin induced by shale gas hydraulic fracturing. *Seismol. Res. Lett.* 90 (5), 1099–1110. doi:10.1785/0220190029

Lin, Q., Cao, P., Wen, G., Meng, J., Cao, R., and Zhao, Z. (2021). Crack coalescence in rock-like specimens with two dissimilar layers and pre-existing double parallel joints under uniaxial compression. *Int. J. Rock Mech. Min. Sci.* 139, 104621. doi:10.1016/j.ijrmms.2021.104621

Lin, Q., Zhang, S., Liu, H., and Shao, Z. (2024). Water saturation effects on the fracturing mechanism of sandstone excavating by TBM disc cutters. *Archives Civ. Mech. Eng.* 24 (3), 154. doi:10.1007/s43452-024-00964-z

Liu, J., Gao, F., Xing, Y., Zheng, W., and Bai, Y. (2023). A new 3d statistical parameter for determining roughness of joint surfaces considering shear direction and asperity features. *KSCE J. Civ. Eng.* 27 (11), 4978–4992. doi:10.1007/s12205-023-1522-x

Liu, R., Zhu, X., Wei, M., Qiao, W., Yu, L., and Hu, M. (2024). Effect of thermal treatment on unloading-induced fracture activation of granites during triaxial shear slip experiments. *J. Rock Mech. Geotechnical Eng.* doi:10.1016/j.jrmge.2024.05.053

Liu, R., Zhu, X., Zhang, Y., Jiang, Y., and Li, S. (2023). Simultaneous unloading of shear and normal stresses induces activation of naturally rough-walled sandstone fractures. *Int. J. Rock Mech. Min. Sci.* 170, 105488. doi:10.1016/j.ijrmms.2023.105488

Loucks, R. G., Reed, R. M., Ruppel, S. C., and Jarvie, D. M. (2009). Morphology, genesis, and distribution of nanometer-scale pores in siliceous mudstones of the Mississippian Barnett shale. *J. Sediment. Res.* 79 (11-12), 848–861. doi:10.2110/jsr.2009.092

Ma, W., and Wang, T. (2020). Numerical study of the influence of joint angle on the failure behavior of randomly and nonpersistently jointed rock mass. *Arabian J. Sci. Eng.* 45 (5), 4023–4036. doi:10.1007/s13369-020-04361-5

Meng, L., McGarr, A., Zhou, L., and Zang, Y. (2019). An investigation of seismicity induced by hydraulic fracturing in the Sichuan Basin of China based on data from a temporary seismic network. *Bull. Seismol. Soc. Am.* 109 (1), 348–357. doi:10.1785/0120180310

Moein, M. J., Langenbruch, C., Schultz, R., Grigoli, F., Ellsworth, W. L., Wang, R., et al. (2023). The physical mechanisms of induced earthquakes. *Nat. Rev. Earth and Environ.* 4 (12), 847–863. doi:10.1038/s43017-023-00497-8

Mohammadi, H., and Pietruszczak, S. (2019). Description of damage process in fractured rocks. *Int. J. Rock Mech. Min. Sci.* 113, 295–302. doi:10.1016/j.ijrmms.2018.12.003

Parchei-Esfahani, M., Gee, B., and Gracie, R. (2020). Dynamic hydraulic stimulation and fracturing from a wellbore using pressure pulsing. *Eng. Fract. Mech.* 235, 107152. doi:10.1016/j.engfracmech.2020.107152

Passelègue, F. X., Brantut, N., and Mitchell, T. M. (2018). Fault reactivation by fluid injection: controls from stress state and injection rate. *Geophys. Res. Lett.* 45 (23), 12–837. doi:10.1029/2018gl080470

Soomro, M. A., Indraratna, B., and Karekal, S. (2022). Critical shear strain and sliding potential of rock joint under cyclic loading. *Transp. Geotech.* 32, 100708. doi:10.1016/j.trgeo.2021.100708

Sun, C., Nie, H., Dang, W., Chen, Q., Zhang, G., Li, W., et al. (2021). Shale gas exploration and development in China: current status, geological challenges, and future directions. *Energy and Fuels* 35 (8), 6359–6379. doi:10.1021/acs.energyfuels.0c04131

Tan, B., He, Z., Fang, Y., and Zhu, L. (2023). Removal of organic pollutants in shale gas fracturing flowback and produced water: a review. *Sci. Total Environ.* 883, 163478. doi:10.1016/j.scitotenv.2023.163478

Tian, W., Yang, S., Dong, J., Cheng, J., and Lu, J. (2022). An experimental study on triaxial failure mechanical behavior of jointed specimens with different JRC. *Geomechanics Eng.* 28 (2), 181–195. doi:10.12989/gae.2022.28.2.181

Wang, B., Verdecchia, A., Kao, H., Harrington, R. M., Liu, Y., and Yu, H. (2021). A study on the largest hydraulic fracturing induced earthquake in Canada: numerical modeling and triggering mechanism. *Bull. Seismol. Soc. Am.* 111 (3), 1392–1404. doi:10.1785/0120200251

Wang, L., Kwiatek, G., Rybacki, E., Bonnelye, A., Bohnhoff, M., and Dresen, G. (2020). Laboratory study on fluid-induced fault slip behavior: the role of fluid pressurization rate. *Geophys. Res. Lett.* 47 (6), e2019GL086627. doi:10.1029/2019gl086627

Wang, Y., Liu, R., Ji, H., Li, S., Yu, L., and Feng, X. (2023). Correlating mechanical properties to fractal dimensions of shales under uniaxial compression tests. *Environ. Earth Sci.* 82 (1), 2. doi:10.1007/s12665-022-10642-z

Wang, Z., Guo, Y., and Wang, M. (2016). Permeability of high-Kn real gas flow in shale and production prediction by pore-scale modeling. *J. Nat. Gas Sci. Eng.* 28, 328–337. doi:10.1016/j.jngse.2015.11.049

Wu, W., Zou, Y., Li, X., and Zhao, J. (2014). An unload-induced direct-shear model for granular gouge friction in rock discontinuities. *Rev. Sci. Instrum.* 85 (9), 093902. doi:10.1063/1.4894207

Xu, Y., Liu, X., Hu, Z., Duan, X., and Chang, J. (2022). Pressure drawdown management strategies for multifractured horizontal wells in shale gas reservoirs: a review. *ACS omega* 7 (17), 14516–14526. doi:10.1021/acsomega.1c05850

Yang, J., Wang, J., and Hu, B. (2023). Numerical analysis of the impacts of multiscale fractures on geothermal reservoir capacity. *J. Energy Eng.* 149 (6), 04023046. doi:10.1061/jleed9.eyeng-4925

Yang, J., Wang, J. G., Liang, W., Li, P., and Sun, R. (2024). Optimal selection of working fluid for enhanced geothermal systems: a comparative analysis of supercritical carbon dioxide and water under various reservoir and extraction conditions. *Appl. Therm. Eng.* 246, 122947. doi:10.1016/j.applthermaleng.2024.122947

Ye, Z., and Ghassemi, A. (2018). Injection-induced shear slip and permeability enhancement in granite fractures. *J. Geophys. Res. Solid Earth* 123 (10), 9009–9032. doi:10.1029/2018jb016045

Ye, Z., and Ghassemi, A. (2020). Heterogeneous fracture slip and aseismic seismic transition in a triaxial injection test. *Geophys. Res. Lett.* 47 (14), e2020GL087739. doi:10.1029/2020gl087739

Ye, Z., Wang, J. G., and Yang, J. (2024). A multi-objective optimization approach for a fault geothermal system based on response surface method. *Geothermics* 117, 102887. doi:10.1016/j.geothermics.2023.102887

Yin, G., Jiang, C., Wang, J. G., and Xu, J. (2015). Geomechanical and flow properties of coal from loading axial stress and unloading confining pressure tests. *Int. J. Rock Mech. Min. Sci.* 76, 155–161. doi:10.1016/j.ijrmms.2015.03.019

Yin, X., Liu, R., Li, S., Zhu, X., Hu, M., and Tan, T. (2024). Tunnel excavation-induced slip properties of faults infilled with grouted sand layer: effect of water content of sands. *KSCE J. Civ. Eng.*, 100092. doi:10.1016/j.kscej.2024.100092

Zeng, Y., Ding, S., Chu, Z., Ma, G., Yang, Z., and Gao, S. (2022). Study on shear slip mechanism of shale gas fractured formation. *Petroleum Sci. Technol.* 40 (9), 1123–1137. doi:10.1080/10916466.2021.2013885

Zhang, F., Cui, L., An, M., Elsworth, D., and He, C. (2022). Frictional stability of Longmaxi shale gouges and its implication for deep seismic potential in the southeastern Sichuan Basin. *Deep Undergr. Sci. Eng.* 1 (1), 3–14. doi:10.1002/dug2.12013

Zhao, Y., Jiang, G., Lei, X., Xu, C., Zhao, B., and Qiao, X. (2023). The 2021 Ms 6.0 Luxian (China) earthquake: blind reverse-fault rupture in deep sedimentary formations likely induced by pressure perturbation from hydraulic fracturing. *Geophys. Res. Lett.* 50 (7), e2023GL103209. doi:10.1029/2023gl103209

Zhou, S., Huang, L., Wang, G., Wang, W., Zhao, R., Sun, X., et al. (2023). A review of the development in shale oil and gas wastewater desalination. *Sci. Total Environ.* 873, 162376. doi:10.1016/j.scitotenv.2023.162376

Zhou, X., Liu, H., Guo, Y., Wang, L., Hou, Z., and Deng, P. (2019). An evaluation method of brittleness characteristics of shale based on the unloading experiment. *Energies* 12 (9), 1779. doi:10.3390/en12091779

Zhu, H., Han, L., Meng, L., Dong, W., and Yan, S. (2022). True triaxial experimental study on fluid flow in single fracture with different dip angles under three-dimensional stress at different depths. *J. Petroleum Sci. Eng.* 211, 110193. doi:10.1016/j.petrol.2022.110193

Zhu, X., Ji, H., Liu, R., Yu, L., and Wang, Y. (2023). Numerical study of hydraulic characteristics of shale fractures during unloading-induced slipping: effects of inclination angle and unloading rate. *Comput. Geotechnics* 164, 105811. doi:10.1016/j.compgeo.2023.105811

Zhu, X., Liu, R., Li, W., Qiao, W., Wei, M., and Yu, L. (2024). Correcting the permeability evaluation of elliptical rock fractures in triaxial shear-flow experiments considering channeling flow. *Rock Mech. Rock Eng.* 57 (2), 1509–1523. doi:10.1007/s00603-023-03601-y